

Article

O₃ Sensitivity and Contributions of Different NMHC Sources in O₃ Formation at Urban and Suburban Sites in Shanghai

Haotian Lin ¹, Ming Wang ^{1,*} , Yusen Duan ^{2,*}, Qingyan Fu ², Wenhao Ji ³, Huxiong Cui ², Dan Jin ², Yanfen Lin ² and Kun Hu ¹

¹ Collaborative Innovation Center of Atmospheric Environment and Equipment Technology, Jiangsu Key Laboratory of Atmospheric Environment Monitoring and Pollution Control, School of Environmental Science and Engineering, Nanjing University of Information Science & Technology, Nanjing 210044, China; 20171207379@nuist.edu.cn (H.L.); meliodas_hu@163.com (K.H.)

² Shanghai Environmental Monitoring Center, Shanghai 200235, China; qingyanf@sheemc.cn (Q.F.); cuihx@sheemc.cn (H.C.); jindan@sheemc.cn (D.J.); linyf@sheemc.cn (Y.L.)

³ Nanjing Intelligent Environmental Science and Technology Co., Ltd., Nanjing 211800, China; jjiwenhao@ies-tech.cn

* Correspondence: wanming@nuist.edu.cn or wangmingmelon@163.com (M.W.); duanys@sheemc.cn or duanys@semc.gov.cn (Y.D.)

Received: 30 January 2020; Accepted: 15 March 2020; Published: 17 March 2020



Abstract: Ground-level ozone (O₃) pollution is still one of the priorities and challenges for air pollution control in the Yangtze River Delta (YRD) region of China. Understanding the relationship of O₃ with its precursors and contributions of different sources in O₃ formation is essential for the development of an O₃ control strategy. This study analyzed O₃ sensitivity to its precursors using a box model based on online observations of O₃, non-methane hydrocarbons (NMHCs), nitrogen oxides (NO_x), and carbon monoxide (CO) at an urban site and a suburban site in Shanghai in July 2017. Anthropogenic sources of NMHCs were identified using the positive matrix factorization (PMF) receptor model, and then contributions of different sources in O₃ formation were estimated by the observation-based model (OBM). The relative incremental reactivity (*RIR*) values calculated by the OBM suggest that O₃ formation at the urban site was in the NMHC-limited regime, while O₃ formation at the suburban site tended between the transition regime and the NMHC-limited regime. Vehicular emission and liquefied petrochemical gas (LPG) use or aged air mass were found to be the two largest contributors at the urban and suburban sites in July, followed by paint and solvent use, and the petrochemical industry. However, from the perspective of O₃ formation, vehicular emission and paint and solvent use were the largest two contributors at two sites due to the higher *RIR* values for paint and solvent use. In addition, the influence of transport on O₃ sensitivity was identified by comparing O₃ sensitivity at the suburban site across two days with different air mass paths. The result revealed that O₃ formation in Shanghai is not only related to local emissions but also influenced by emissions from neighboring provinces. These findings on O₃–NMHC–NO_x sensitivity, contributions of different sources in O₃ formation, and influence of transport could be useful for O₃ pollution control in the YRD region. Nevertheless, more quantitative analyses on transport and further evaluation of the uncertainty of the OBM are still needed in future.

Keywords: O₃; OBM; volatile organic compounds (VOCs); PMF; Shanghai

1. Introduction

Ground-level ozone (O_3) pollution in China is becoming of increasing concern in recent years. The China Environment Report [1] showed that the 90th percentile for the daily maximum 8-h moving average (DMA-8h) O_3 concentration for 74 major cities in China increased from $139 \mu\text{g}/\text{m}^3$ to $169 \mu\text{g}/\text{m}^3$ during 2013–2017 (<http://datacenter.mee.gov.cn>). The Beijing–Tianjin–Hebei (BTH) region, the Yangtze River Delta (YRD), and the Pearl River Delta (PRD) are the most severe O_3 pollution areas in China, with respective 90th percentile DMA-8h O_3 concentrations of $193 \mu\text{g}/\text{m}^3$, $170 \mu\text{g}/\text{m}^3$, and $165 \mu\text{g}/\text{m}^3$ in 2017 [1]. Additionally, a significant increase in O_3 concentrations in these three regions was reported by previous studies [2]. The summer DMA-8h O_3 trends for the BTH, YRD, and PRD regions were $3.1 \text{ ppbV}\cdot\text{year}^{-1}$, $2.3 \text{ ppbV}\cdot\text{year}^{-1}$, and $0.56 \text{ ppbV}\cdot\text{year}^{-1}$ during 2013–2017 [1]. Compared with 2016, the 90th percentile of the DMA-8h O_3 concentration for Shanghai increased by 10.4% in 2017, which was faster than that for Guangzhou (4.5%) and Beijing (−3%) [1].

In the urban atmosphere, O_3 mainly comes from the photochemical production of volatile organic compounds (VOCs) and nitrogen oxygen (NO_x) [3]. Understanding the relationship of O_3 formation with VOCs and NO_x is essential for O_3 control. Until now, several methods were developed to investigate O_3 –VOC– NO_x sensitivity, such as VOCs/ NO_x [4], a linear regression analysis of O_3 with its precursors [5], air quality model based on emissions (EBM) [6], and a box model based on observations (OBM) [7]. Since O_3 -related chemical reactions are highly simplified in the VOCs/ NO_x and linear regression methods, these two methods are usually used to preliminarily identify O_3 sensitivity. Large uncertainties of emission inventories for O_3 precursors (especially VOCs) in China were reported by several studies [8,9]. Considering that inaccurate emission data of VOCs and NO_x would bias O_3 –VOC– NO_x sensitivity results, many studies in China applied the OBM to investigate the relationship of O_3 with its precursors [10,11].

Ambient VOCs can be emitted into the atmosphere from anthropogenic and biogenic sources, such as vehicular exhaust, fuel evaporation, coal burning, biomass burning, building painting, asphalt application, the petrochemical industry, and so on [12]. Understanding the sources of VOCs is a basic step toward developing control measures for VOC reduction and O_3 control strategies in those regions where O_3 formation is controlled by VOCs. Some O_3 sensitivity and VOC source analysis studies based on measurements were conducted in the YRD region. Two studies used VOCs/ NO_x measured at urban sites in Shanghai to analyze O_3 sensitivity, and they suggested that O_3 formation was mainly controlled by VOCs (i.e., a VOC-limited regime) [13,14]. The OBM study by Tan et al. [15] also suggested that O_3 formation at an urban site in Shanghai was in a VOC-limited regime. The VOCs source apportionment studies by receptor models suggested that vehicular emission and industrial emissions were important sources for VOC mixing ratios at an urban site in Shanghai [16,17]. However, few studies combining VOC source apportionment with O_3 sensitivity results were conducted in Shanghai to estimate the contribution of different VOC sources to O_3 formation.

In this study, O_3 sensitivity to its precursors was analyzed using an OBM based on online measurements of O_3 , non-methane hydrocarbons (NMHCs), NO_x , and CO at an urban and a suburban site in Shanghai in July 2017. Anthropogenic NMHC sources at these sites were apportioned using the positive matrix factorization (PMF) model. Contributions of different PMF-resolved NMHC sources in O_3 formation were then estimated using the OBM combined with PMF results. Furthermore, trajectory analysis was conducted to evaluate the influence of transport in a case study.

2. Methodology

2.1. Measurements

The measurements of O_3 , NO_x , and non-methane hydrocarbons (NMHCs) were conducted at the Pudong site (121.53° north (N), 31.23° east (E)) (PD) and the Dianshanhu site (120.98° N, 31.09° E) (DSH) from 1 July to 31 July. The locations of these two sites are shown in Figure 1. The PD site is located in the Pudong environmental monitoring station in the urban area of Shanghai. Two main roads,

the Yanggao Middle Road and Century Avenue, are located about 300 m southwest and southeast of this site. The largest coastal port (Shanghai Port) in Shanghai is located about 19 km east of the PD site; meanwhile, the largest petrochemical complex zone (Jinshan) is located about 50 km southwest of the PD site. The DSH site is situated in the west suburban area of Shanghai, about 55 km west of the PD site. A highway (G50) is located in this area, 500 m southwest of the DSH site.

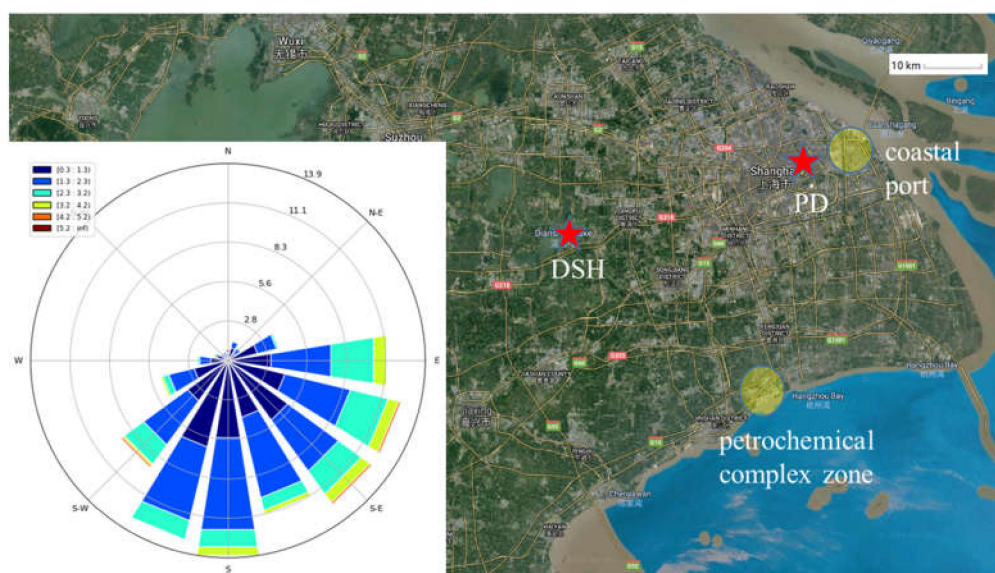


Figure 1. Map of the Pudong (PD) and Dianshanhu (DSH) sites in Shanghai. The wind rose in the bottom left shows the probability of wind speeds and directions in Shanghai from 1–31 July 2017.

The ambient measurement data of O_3 , NO_x , and CO were provided by the Shanghai Environmental Monitoring Center. Briefly, ambient O_3 was determined using a commercial ultraviolet absorption spectrometer (Model 49i, Thermo Fisher Scientific Inc., Waltham, MA, USA). Ambient NO_x and CO were detected using a chemiluminescence system (Model 42i-TL, Thermo Fisher Scientific Inc., Waltham, MA, USA) and infrared absorption spectrometry (Model 48i, Thermo Fisher Scientific Inc., Waltham, MA, USA), respectively. The meteorological data, including temperature, wind direction and speed, relative humidity, and pressure, were provided by the Shanghai Meteorological Bureau.

Ambient levels of 56 C2–C12 non-methane hydrocarbons (NMHCs) at the PD and DSH sites were measured online using commercial gas chromatography (GC) systems. The principles of NMHC sampling, pre-concentration, and detection for these two GC systems were similar. Firstly, ambient air was sampled in the analysis system using a Teflon tube, while target compounds were enriched through an adsorbent tube at room temperature or at low temperature. After sampling, the adsorbent tube was rapidly heated, and the concentrated NMHCs were desorbed and injected into GC for separation and detection.

A GC-955 611/811 series was used to measure the NMHCs at the PD site (Synspec Inc., Groningen, Netherlands). The enrichment temperature was set as $-5\text{ }^\circ\text{C}$. The 611 series was designed to measure C6–C12 NMHCs. A photo ionization detector (PID) and flame ionization detector (FID) were used to quantify the NMHCs. The 811 series was used for monitoring C2–C5 NMHCs, with a PID and FID dual detector. The resolution of the 611 series and 811 series monitoring time was 0.5 h. A more detailed description of this system can be found in the Reference [18].

The ambient NMHCs at the DSH site were also measured using an online GC system (GC-866, Chromatotec Inc., Saint-Antoine, France), with a time resolution of 0.5 h. The instrument consists of two independent sampling and analysis systems: one is a low-boiling-point NMHC sampling system (C2–C5), and the other is a high-boiling-point NMHC sampling system (C6–C12). The pre-concentration temperature for the low-carbon analyzer was set as $-10\text{ }^\circ\text{C}$, while the pre-concentration system for the

high-carbon analyzer was at room temperature. The detectors for the low-carbon and high-carbons analyzers were FIDs.

Quality assurance and quality control (QA/QC) procedures were carried out to ensure the quality of the NMHC data. Firstly, before monitoring, we used US Environmental Protection Agency (U.S. EPA) approved standard gas for calibration and the five-point calibration method to calibrate and check the instrument; the correlation coefficients were above 0.99. Secondly, we performed daily maintenance, single-point calibration and peak-window drift calibration, and data correction every week. Thirdly, the GC-866 was calibrated daily with butane, hexane, and benzene. The deviation of the calibration point did not exceed 10%.

2.2. Positive Matrix Factorization Model

The positive matrix factorization (PMF) model uses mathematical methods to decompose a concentration matrix x into two matrices, g and f , and a residual matrix, e (Equation (1)) [19,20].

$$x_{ij} = \sum_{k=1}^p g_{ik}f_{kj} + e_{ij} \quad (1)$$

where p is the number of pollution sources, x_{ij} represents the concentration of the j component in the i sample, g_{ik} represents the contribution of the k source to the i sample, f_{kj} is the content of the j component in the k source, and e_{ij} is the residual for each species.

2.3. Observation-Based Model

An observation-based model (OBM) coupled with a Carbon-Bond IV mechanism developed by Cardelino and Chameides [21] was used to simulate the atmospheric chemical process under the constraint of the hourly measured concentrations of NO, NMHCs, and CO. The integral of the O₃ production rate over time during the daytime (7:00 a.m.–7:00 p.m.) was calculated as the O₃ formation potential (P_{O₃}). Since O₃ can react with NO quickly to produce NO₂ in an urban atmosphere and NO₂ can then produce O₃ by photolysis, the total amounts of P_{O₃} and NO consumption (P_{O₃-NO}) were applied to discussions on O₃ sensitivity. More detailed descriptions on the OBM model can be found in the Supplementary Materials.

This model also calculated the sensitivity of P_{O₃-NO} to changes in the concentration of each precursor (Equation (2)), i.e., the relative incremental reactivity (RIR).

$$RIR^i(X) = \frac{(P_{O_3-NO}^i(X) - P_{O_3-NO}^i(X - \Delta X)) / P_{O_3-NO}^i(X)}{\Delta S(X) / S(X)} \quad (2)$$

where $S(X)$ represents the concentration of precursor X emitted or transported to the measurement site, ΔX is the change in X concentration caused by a hypothetical change in $S(X)$, and superscript i is used to denote the specific site where the measurements were made. $P_{O_3-NO(X)}^i$ represents the O₃ formation potential for the i measurement, which is the net O₃ production plus NO consumed during the evaluation period.

Relative contributions of each PMF-resolved source (F_i) to O₃ formation were calculated using Equation (3) [7].

$$Relative\ contribution(F_i) = \frac{RIR(F_i) \times Concentration(F_i)}{\sum_{i=1}^N RIR(F_i) \times Concentration(F_i)} \times \% \quad (3)$$

where $Concentration(F_i)$ means the summed concentration of fitting species in the i -th PMF-resolved factor, $RIR(F_i)$ represents the relative increment of P_{O₃-NO} when concentrations of all fitting species in the i -th PMF-resolved factor were reduced by 10%, and N means the total number of PMF-resolved factors.

3. Results and Discussion

3.1. O₃ Pollution Characteristics

The hourly average O₃ (1h O₃) concentrations during 1–31 July 2017 at the PD site and the DSH site were in the range of 0.9–169.4 ppbV and 0.5–167.5 ppbV, respectively (Figure 2). The DMA-1h O₃ concentration at the PD site and the DSH site ranged from 30.3 ppbV to 167.5 ppbV and from 35.9 ppbV to 169.4 ppbV, respectively. The DMA-8h O₃ concentrations at the PD site ranged from 28 ppbV to 131 ppbV, while the DMA-8h O₃ concentrations for the DSH site ranged from 30 ppbV to 140 ppbV. There were 18 days at the PD site and 19 days at the DSH site exceeding the national grade II ambient air quality standard (93.3 ppbV for DMA-1h O₃ and 74.7 ppbV for DMA-8h O₃).

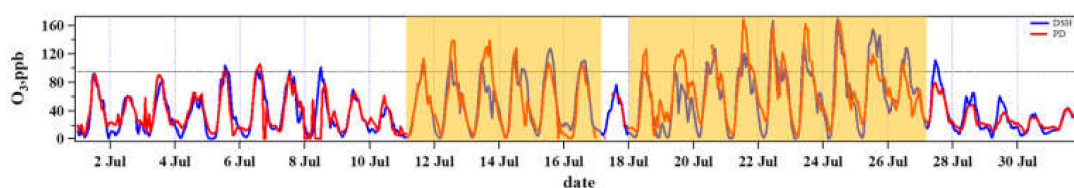


Figure 2. Time series of the hourly average O₃ concentrations at the DSH (blue line) and PD (red line) sites from 1–31 July 2017. The horizontal black dotted line means the national grade II standard for daily maximum 1-h moving average (DMA-1h) O₃ (200 µg/m³, i.e., 93.3 ppbV). The areas shaded by orange represent two O₃ pollution episodes (11–16 and 18–26 July).

The diurnal variation patterns of 1-h O₃ concentrations at the PD site and the DSH site were similar (Figure 3a), with maximum values occurring from 12:00–1:00 p.m. and the minimum value appearing at 5:00 a.m. Since Shanghai is a coastal city where meteorological conditions are complicated, high-level ozone on some days is not from local photochemical formation but transport [22,23]. This suggests that O₃ formation occurred mainly due to photochemical production during July 2017. In contrast with O₃, anthropogenic NMHCs and NO_x showed higher concentrations at night and during the morning (Figure 3b,c). The maximum diurnal variation patterns of hourly averaged anthropogenic NMHCs and NO_x concentrations occurred at 5:00–8:00 a.m., and the minimum value appeared at 11:00 a.m.–2:00 p.m. The NO_x concentrations were in the range of 3.9–104.2 ppbV and 1.9–113.9 ppbV at the DSH site and the PD site, respectively. The anthropogenic NMHCs concentration ranged from 2.1 ppbV to 80.1 ppbV at the DSH site, while it ranged from 4.1 ppbV to 130.7 ppbV at the PD site. The average mixing ratios of anthropogenic NMHCs and NO_x at the PD sites and DSH sites were 22.7 ppbV and 18.5 ppbV, and 17.6 ppbV and 21.4 ppbV, respectively. The average anthropogenic NMHCs concentration at the PD site was higher than that at the DSH site, while the average NO_x concentration was lower than that at the DSH site.

3.2. O₃ Formation Sensitivity to Its Precursors during Pollution Episodes

From 1–31 July, there were 17 days with O₃ exceeding the national grade II air quality standard at both the PD and the DSH sites. In addition to the 15 days we selected as O₃ pollution episodes, O₃ concentrations on 5 and 6 July also exceeded the threshold. However, the O₃ concentrations at 6:00–7:00 p.m. on 7 July and NMHC concentrations at 4:00 p.m. were missing due to the calibration of measurement instruments; therefore, 15 days (11–16 July and 18–26 July) were selected to analyze O₃ sensitivity. From 11–16 July, DMA-8h O₃ reached 107–127 ppbV at the DSH site and 102–138 ppbV at the PD site. From 18–26 July, DMA-8h O₃ reached 94–169 ppbV at the DSH site and 106–168 ppbV at the PD site. The sensitivity of O₃ to NMHCs and NO_x during these two episodes was analyzed by the OBM.

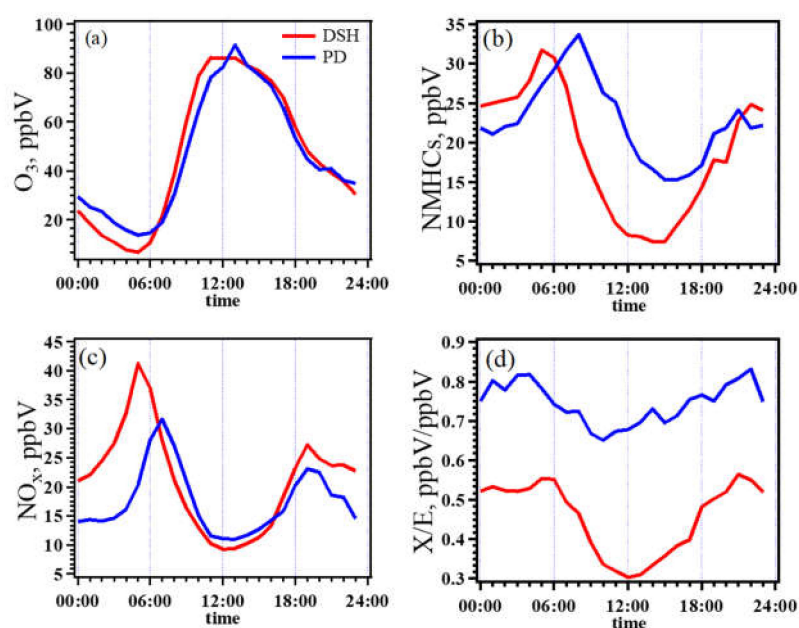


Figure 3. Mean diurnal variations of the measured ambient levels for (a) O₃, (b) non-methane hydrocarbons (NMHCs), (c) NO_x, and (d) ratios of *o*-xylene to ethylbenzene (X/E) at the DSH site (red line) and PD site (blue line) from 1–31 July 2017.

3.2.1. Model Performance Evaluation: OH and HO₂ Simulation

The OBM-simulated concentrations of OH and HO₂ radicals during the pollution period were compared with measurements to evaluate the performance of OBM. Detailed descriptions on OH and HO₂ simulation are provided in the Supplementary Materials. As shown in Figure 4, the OBM-modeled OH and HO₂ concentrations both displayed a diurnal pattern, with the maximum occurring at about 12:00–1:00 p.m., which is similar to the results in Shanghai [15]. The average daily maximum OBM-modeled OH and HO₂ concentrations at these two sites were $(2.16\text{--}2.52) \times 10^7$ molecules·cm^{−3} and $(2.36\text{--}3.37) \times 10^9$ molecules·cm^{−3}, respectively. These results agree well with the OH and HO₂ radical concentrations in Shanghai (1.02×10^7 molecules·cm^{−3}) [24]. Shanghai was reported by previous studies to have respective values of $(3\text{--}26) \times 10^6$ molecules·cm^{−3} and $(2\text{--}25) \times 10^8$ molecules·cm^{−3} for OBM simulations and field observations [15,24–28].

To further check the simulated OH concentrations by the OBM, the daily average OH was also estimated based on the ratios of two hydrocarbons that have similar emission ratios but different reaction rates [8]. In this study, the ratio of *o*-xylene to ethylbenzene (X/E) was used to calculate OH. The average diurnal variation patterns of X/E at the DSH and PD from 11–16 July and from July 18–26 in 2017 at the two sites are shown in Figure 3d. It can be seen that X/E showed higher values at night and in the early morning, indicating that the air masses were relatively fresh. From 5:00–6:00 a.m., X/E gradually decreased with photochemical reaction processing, reaching its minimum value at noon.

$$[OH]\Delta t = \frac{1}{(k_X - k_E)} \times \left[\ln \frac{[X]}{[E]}_{t=0} - \ln \frac{[X]}{[E]} \right] \quad (4)$$

where k_X and k_E are the reaction rate constants of *o*-xylene (13.6×10^{-12} cm³·molecule^{−1}·s^{−1}) and ethylbenzene (7.1×10^{-12} cm³·molecule^{−1}·s^{−1}), respectively [29]. $[X]/[E]_{t=0}$ is the average ratio of $[X]/[E]$ at 5:00 a.m., with respective values of 0.55 ppbV/ppbV and 0.78 ppbV/ppbV at the DSH and PD sites. $[X]/[E]$ is the daily minimum ratio of *o*-xylene to ethylbenzene, with respective values of 0.30 ppbV/ppbV and 0.65 ppbV/ppbV at the DSH and the PD site, respectively. Since these sites were close to emission sources, the aging of air masses was inevitably influenced by continuous fresh emissions [30]. The air mass ages of Shanghai were calculated based on NO_x/NO_y measurements

and WRF-Chem simulations in the study by Tie et al. that suggested the air mass ages at the PD site ranged from 0–1 h from August–September 2009 [31]. Therefore, the Δt value at the PD site was set as 0.5 h. The DSH site was 55 km away from the PD site; therefore, its average air age was set as 1 h. The daily average OH concentrations were then calculated as 2.54×10^7 molecule·cm⁻³ and 1.25×10^7 molecule·cm⁻³.

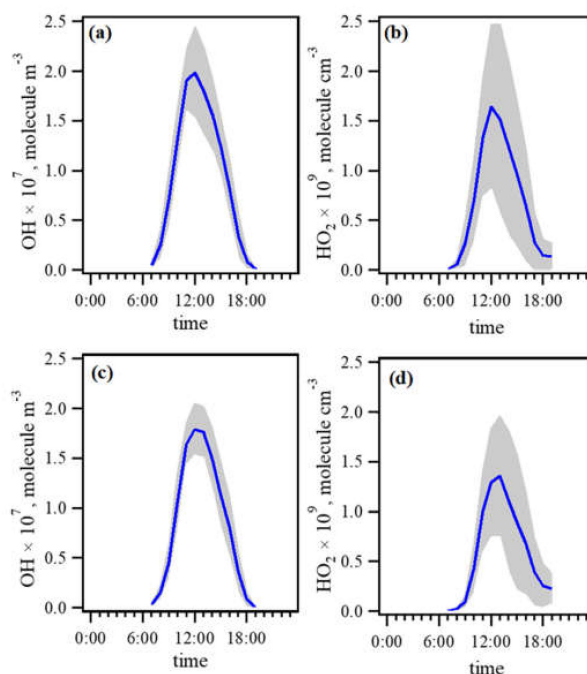


Figure 4. Mean diurnal variations of the OH and HO₂ concentrations for (a,b) the DSH site and (c,d) the PD site during pollution episodes (11–16 July and 18–26 July) simulated using the observation-based model (OBM). The shaded gray areas represent the standard deviation of simulated radical concentrations at each hour.

3.2.2. O₃–NMHC–NO_x Sensitivity at the PD and DSH Sites

Figure 5 shows the average *RIR* values for NO_x, anthropogenic hydrocarbons (AHCs), biogenic hydrocarbon (NHC, isoprene in this study), and CO at the PD and DSH sites during two O₃ pollution episodes (11–16 July and 18–26 July) calculated using the OBM. A positive *RIR* value for a precursor indicates that reducing this compound will lead to a decrease in O₃ production, while a negative *RIR* value for a precursor indicates that reducing this compound will result in an increase in O₃ formation [21]. The *RIR* values for AHC (*RIR*(AHC)) and NHC (*RIR*(NHC)) were both positive at these two sites, suggesting that reducing AHC and/or NHC would result in O₃ decrease during O₃ pollution episodes. The average *RIR*(AHC) at the DSH site was 0.26%/%, slightly lower than the value of *RIR*(NHC) (0.30%/%). The *RIR*(AHC) and *RIR*(NHC) for the PD site were higher than those for the DSH site, with respective values of 0.44%/% and 0.36%/%. It should be noted that the *RIR*(NHC) values are comparable with *RIR*(AHC) at both sites. This implies NHC also played an important role in O₃ formation. However, NHC emission is hard to control. The average *RIR* value for NO_x (*RIR*(NO_x)) at the DSH site was 0.07%/%, which means that reducing NO_x would be beneficial for O₃ control. Considering that the average *RIR*(AHC) and *RIR*(NO_x) at the DSH site were both positive, O₃ formation during pollution episodes at this site was controlled by both AHC and NO_x, i.e., in the transition regime. Unlike the DSH site, the average *RIR*(NO_x) at the PD site was negative, with a value of −0.11%/%. This means that reducing NO_x would result in an O₃ increase; therefore, O₃ formation at this site is in an NO_x-titration regime, i.e., NMHC-limited regime.

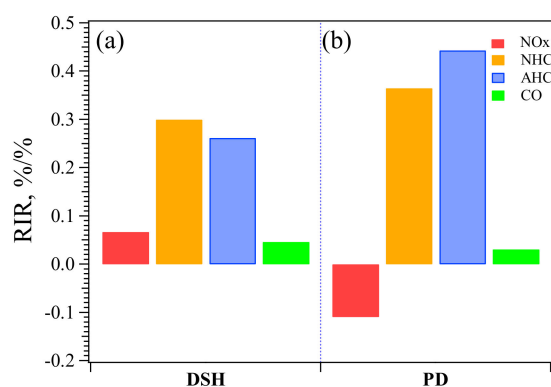


Figure 5. Average relative incremental reactivity (*RIR*) values of the O₃ precursors NO_x, anthropogenic hydrocarbons (AHCs), biogenic hydrocarbons (NHCs), and CO at (a) the DSH site and (b) the PD site from 11–26 July.

Figure 6 shows the temporal variations of *RIR* values for each precursor at the DSH site and the PD site from 11–26 July. At the DSH site, the *RIR*(AHC) ranged from 0.62%/ to 0.83%/ from 11–14 July; meanwhile, the *RIR* (NO_x) was in the range of −0.53%/ to −0.14%/ . This suggests that the O₃ formation during this period was in a highly NMHC-limited regime (i.e., an NO titration regime). However, from 15–20 July, the *RIR*(AHC) dropped to 0.04%/–0.29%/ , while the *RIR*(NO_x) increased to 0.01%/–0.31%/ . This means that O₃ formation was controlled by both NMHCs and NO_x (i.e., in a transition regime). At the PD site, the *RIR*(AHC) and *RIR*(NO_x) values were in the range of 0.11%/–0.30%/ and −0.13%/–0.12%/ , respectively, from 11–16 July. The differences between the maximum and minimum values of *RIR*(AHC) and *RIR*(NO_x) at the PD site were 0.25%/ and 0.19%/ , respectively, lower than their differences at the DSH site (0.79%/ for *RIR*(AHC) and 0.53%/ for *RIR*(NO_x)).

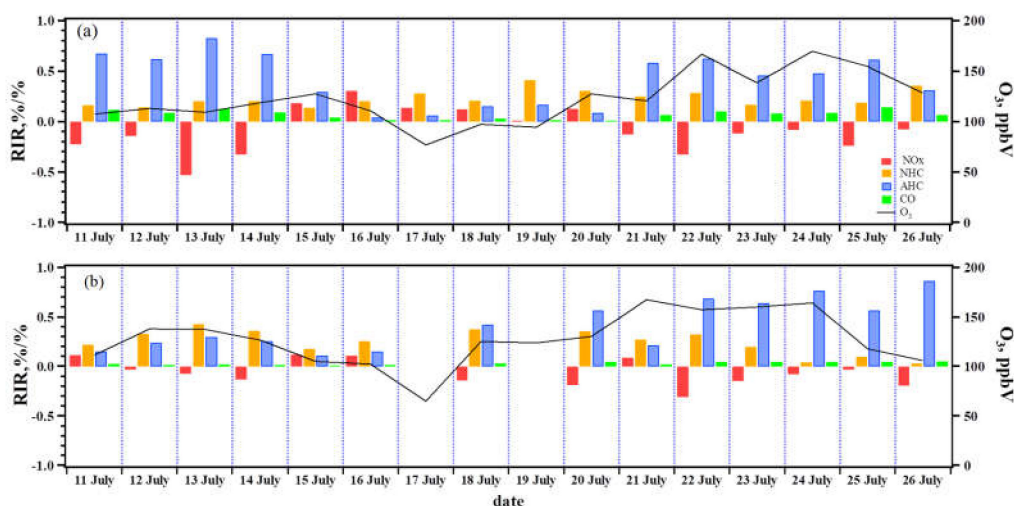


Figure 6. Variations of *RIR* values for NO_x (red bar), NHC (orange bar), AHC (blue bar), and CO (green bar) and DMA-1h O₃ levels (black line) at (a) the DSH site and (b) the PD site from 11–26 July 2017.

We summarized O₃ sensitivity studies in Shanghai from 2006 to 2017 (Table 1). In urban regions, O₃ sensitivity analyses using OBM [15,32,33], the air quality model based on emissions (EBM) [6,34,35], and VOCs/NO_x ratios [13,14] all suggested that O₃ formation was in a VOC-limited regime. The O₃ formation at the PD site determined by the OBM in this study was also in a VOC-limited regime. It can be found that O₃ sensitivity in urban areas of Shanghai agreed well among different studies. However, O₃ formation regimes in suburban/rural regions from previous studies disagreed. The OBM study

by Xue et al. [36] suggested that O₃ formation at a suburban site in May 2005 was in a VOC-limited regime. However, two air quality studies suggested that O₃ formation in suburban areas of Shanghai were in a NO_x-limited regime during the summers of 2007 and 2010. Unlike previous studies, O₃ formation at the suburban site (DSH) determined by the OBM in this study was in a transition regime. The discrepancy in O₃ formation regimes in suburban/rural regions among different studies may be related to long-term changes of O₃ precursors. Industrial VOC emission increased rapidly during recent years [37]; therefore, VOCs/NO_x tended to increase, resulting in O₃ formation being more sensitive to NO_x [38]. It should be pointed out that there is a large uncertainty in the discussion of long-term temporal variations of O₃ sensitivity since these studies used different methods based on measurements at different sites. O₃ sensitivity analysis based on long-term measurements at the same site is needed to investigate temporal changes of O₃ formation regimes.

Table 1. Summary of the studies of O₃ formation regime in Shanghai. VOC—volatile organic carbon.

Land-Use Function	Time	Method	O ₃ Formation Regime	Reference
Urban	January 2006–May 2007	OBM	VOC-limited	Geng et al., 2008 [32]
	15 June 2006–14 June 2007	VOC/NO _x ratio	VOC-limited	Ran et al., 2009 [14]
	20 July–30 July 2007	EBM	VOC-limited	Li et al., 2011 [34]
	2 August–11 August 2007	EBM	VOC-limited	Tie et al., 2009 [35]
	July–August 2009	OBM	VOC-limited	Ran et al., 2012 [33]
	November–December 2009	VOC/NO _x ratio	VOC-limited	Tang et al., 2008 [13]
	5 August–31 August 2010	EBM	VOC-limited	Li et al., 2012 [6]
	21 August–02 Sep 2016	OBM	VOC-limited	Tan et al., 2019 [15]
11 July–26 July 2017	OBM	VOC-limited	This study	
Suburban	4 May–01 June 2005	OBM	VOC-limited	Xue et al., 2014 [36]
	20 July–30 July 2007	EBM	NO _x -limited	Li et al., 2011 [34]
	5 August–31 August 2010	EBM	NO _x -limited	Li et al., 2012 [6]
	11 July–26 July 2017	OBM	Transition regime	This study

3.2.3. Impact of Gaseous Nitrous Acid (HONO) on OBM-Derived O₃ Formation Regime

The photolysis of HONO is an important source of OH radicals in the pollutant boundary layer [39]. In this study, HONO measurements were not conducted. Relatively good correlations between HONO and NO_x in different field measurements were reported by Elshorbany et al. [40], and the average ratios for HONO versus NO_x (HONO/NO_x) were 0.017 ± 0.003 ppbV/ppbV and 0.042 ± 0.01 ppb/ppb for measurements campaigns with low HONO/NO_x (<0.02 ppbV/ppbV) and high HONO/NO_x ratios (>0.02 ppbV/ppbV), respectively. To evaluate the uncertainty of *RIR* calculation caused by HONO, HONO concentrations were assumed as 1%, 2%, and 4% of the observed NO_x concentrations and then applied to constrain the OBM.

As shown in Figure 7, the *RIR* values for NHC, AHC, and CO tended to decrease with increasing HONO concentrations at both sites. At the DSH site, when the 1% NO_x concentration was input to the OBM as the HONO concentration, the *RIR*(NO_x) decreased from 0.069%/ to 0.040%/ . With the rise of assumed HONO concentration from 2% to 4% of NO_x concentration, the *RIR* (NO_x) increased from 0.040%/ to 0.048 %/ . At the PD site, when the 1% of NO_x concentration was used as the HONO concentration, the *RIR*(NO_x) decreased from −0.11%/ to −0.13%/ . Then, with the rise of HONO concentration, *RIR*(NO_x) increased from −0.13%/ to −0.03%/ . Although the O₃ formation regimes did not change at both sites, the variations of *RIR* values with HONO concentrations suggest the important influence of HONO concentration on the calculation of *RIR* values for O₃ precursors by the OBM. Therefore, to reduce the uncertainty of OBM-derived O₃ sensitivity, measurements of HONO are needed.

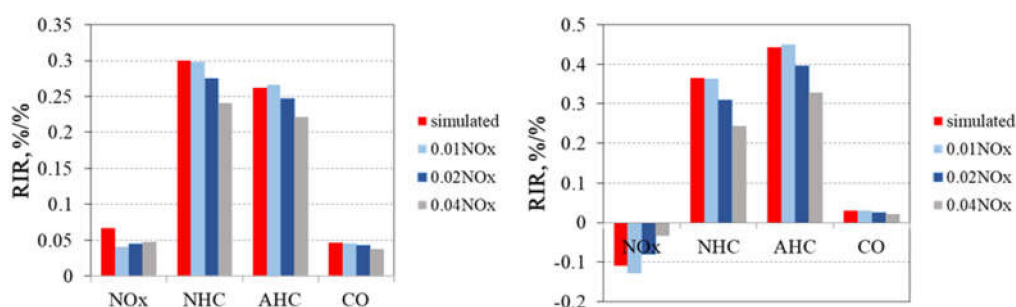


Figure 7. The average *RIR* values for NO_x, NHC, AHC, and CO for simulated gaseous nitrous acid (HONO) (red bar) and HONO concentrations assumed as 1% (pale-blue bar), 2% (dark-blue bar), and 4% (gray bar) of NO_x concentrations at the DSH site (left panel) and the PD site (right panel).

3.2.4. Key Anthropogenic NMHC Species in O₃ Formation

To identify key hydrocarbon species in O₃ formation at the DSH and PD sites during pollution episodes, the *RIR* values for individual anthropogenic hydrocarbons were calculated based on measured chemical compositions of NMHCs by the OBM model. Figure 8 shows the top 10 anthropogenic hydrocarbon species with largest *RIR* values at these two sites. It can be found that the top 10 species were rather consistent at the two sites, even though their ranking showed some differences. Xylenes, propene, trans/cis-butene, propane, ethene, and 1,2,3-trimethylbenzene were the most important species in O₃ formation. The difference in *RIR* value ranking for each hydrocarbon between the two sites was possibly related to the difference in levels and chemical compositions of hydrocarbon species between these two sites.

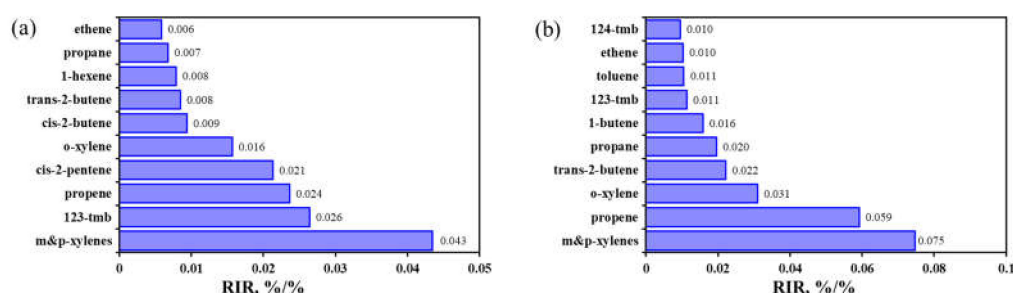


Figure 8. Species with the top ten relative incremental reactivity (*RIR*) values at the (a) DSH and (b) PD sites.

3.3. Contributions from Different Anthropogenic Sources on O₃ Formation

3.3.1. Source Apportionment of NMHCs by the PMF Model

Ambient NMHC source apportionments were determined using the PMF model based on 554 samples measured at the DSH site from 1 July to 31 July. Twenty-three species with high mixing ratios and measurement accuracy, as well as large contributions in O₃ formation, were selected as input for the PMF model. We tested 3–8 factor resolutions of PMF, and the four-factor result was selected to explain the local NMHC sources. Figure 9a shows the chemical profiles of 23 NMHCs for the four PMF-resolved factors at the DSH site. The bar indicates the percentage of each species in the total mixing ratios of 23 species for this factor. The black-filled diamond indicates the relative contribution of each factor in the measured mixing ratio of individual species.

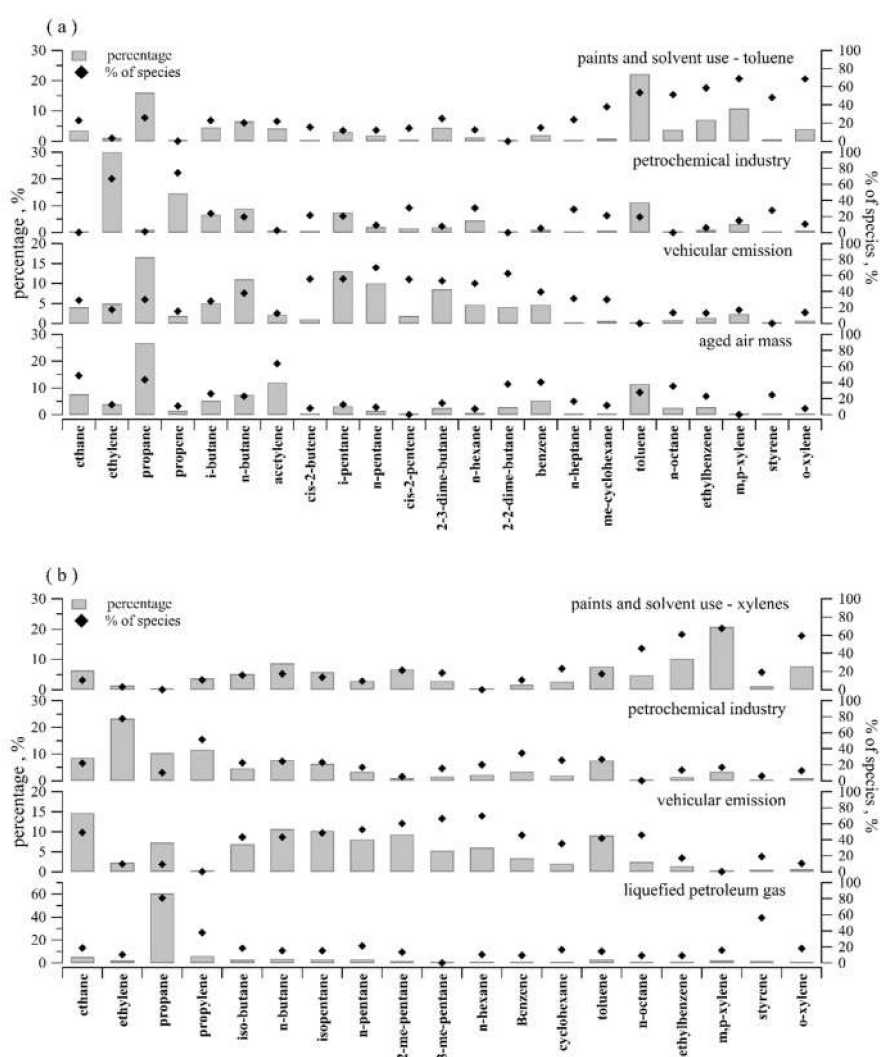


Figure 9. Chemical profiles of NMHCs for individual positive matrix factorization (PMF)-resolved factors at (a) the DSH site and (b) the PD site from 1–31 July 2017. The bar represents the percentage of individual species in the total mixing ratios for all fitting species. The black-filled diamond indicates the relative contribution of each factor in the measured mixing ratio of individual species.

C7–C8 aromatics were the most abundant species in Factor 1, with 47% of total mixing ratios of 23 NMHCs species. Several studies in China reported that C7–C8 aromatics were the most important compounds in NMHCs emitted from paints and solvent [41,42]; therefore, Factor 1 was considered a source related to paint and solvent use. Factor 2 was characterized by its high relative contributions to ethylene (30%) and propylene (15%). Light alkenes are characteristic species NMHCs from the petrochemical industry [43]; thus, Factor 2 was identified as the petrochemical industry. C4–C5 alkanes and alkenes were the most important species in Factor 3, with 42%. C4–C5 hydrocarbons are major constituents of NMHCs from vehicular exhaust and gasoline evaporation [12,44]; thus, this factor was identified as vehicular emission. The dominant components in Factor 4 were long-lived species (e.g., ethane, propane, acetylene, and benzene); thus, this factor was considered as aged air masses.

NMHC source apportionments at the PD site were determined based on 494 samples measured in July. Nineteen species were input into the PMF model. The factor number was also set as four. Figure 9b shows the chemical profiles of the NMHCs for the four PMF-resolved factors at the PD site. Similar to Factor 1 at the DSH site, the main components in Factor 1 at the PD site were also C7–C8 aromatics; thus, this factor was considered as paint and solvent use. It should be pointed out that Factor 1 at these two sites did not represent a totally identical source, since toluene was the major

constitute in Factor 1 at the DSH site, while m,p-xylene was the most important species in Factor 1 at the PD site. To avoid confusion caused by the same name, Factor 1 at the DSH and PD sites was named paint and solvent use-toluene and paint and solvent use-xylene, respectively. Factor 2 at the PD site was characterized by its high contributions to ethylene (23%) and propylene (12%); thus, this factor was identified as the petrochemical industry. Factor 3 was characterized by C4–C5 alkanes and alkenes, which were influenced largely by vehicular emissions in urban areas [12,44]; thus, this factor was recognized as vehicular emissions. Compared with Factor 3 at the DSH site, the percentage of ethane in Factor 3 at the PD site was significantly higher. One possible explanation for this is that a large number of buses and taxis in Shanghai use compressed natural gas (CNG) or liquefied natural gas (LNG) as fuels [45], and ethane is the main component of natural gas [46]; therefore, a part of ethane was attributed to the vehicular emission factor at the PD site. The dominant component in Factor 4 was propane, with 60%. Propane is the most abundant species in liquefied petroleum gasoline (LPG) [47]; thus, Factor 4 was identified as LPG use.

The relative contributions of different sources to total mixing ratios of NMHCs species that were input into PMF are shown in Figure 10. At the DSH site, aged air mass contributed 32% of the NMHC mixing ratios, followed by vehicular emissions (30%), paint and solvent use–toluene (24%), and the petrochemical industry (14%). At the PD site, the largest two contributors to NMHCs were liquefied petroleum gas (LPG) use (33%) and vehicular emissions (30%), followed by paint and solvent use–xylenes (21%) and the petrochemical industry (16%).

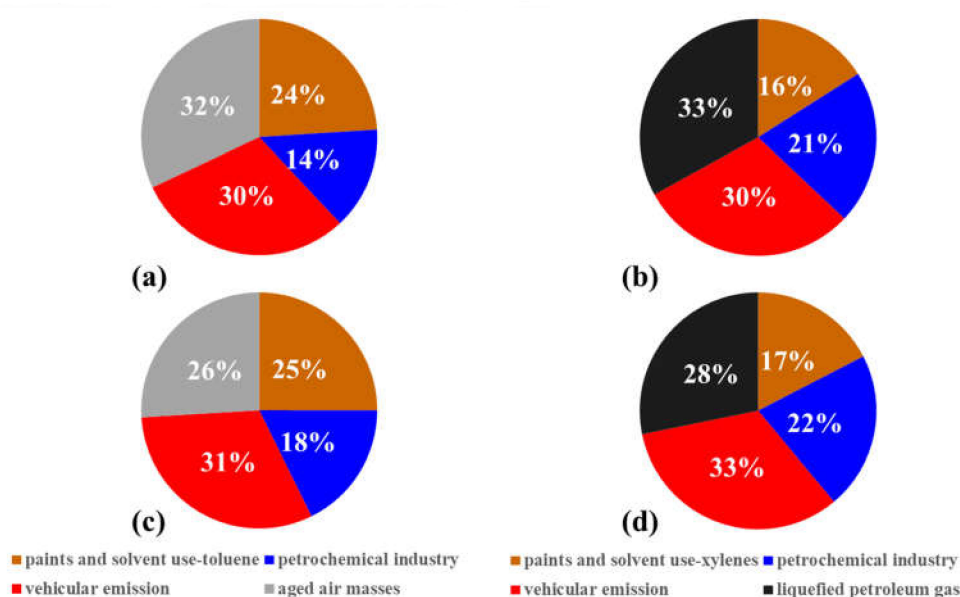


Figure 10. Relative contributions of different sources to NMHCs mixing ratios from (a,b) 1–31 July and (c,d) O₃ pollution episodes (a,c) at the DSH site and (b,d) the PD site.

3.3.2. Contributions of Anthropogenic NMHCs Sources in O₃ Formation

To estimate contributions of different anthropogenic NMHCs sources in O₃ photochemical production, the PMF-resolved NMHCs concentrations for different sources were input into the OBM to calculate *RIR* values for each source. The *RIR* values for different NMHCs sources at the DSH site and PD site during O₃ pollution episodes (11–16 July and 17–26 July) are shown in Figure 11a,b. Among the four sources at the DSH site, the *RIR* values for paint and solvent use-toluene and vehicular emission were close, with a value of 0.22%/%, slightly higher than that for the petrochemical industry (0.20%/%), and significantly higher than that for aged air mass (0.08%/%). At the PD site, the largest *RIR* value was from paint and solvent use-xylenes (0.31%/%), followed by the petrochemical industry (0.27%/%), vehicular emission (0.21%/%), and LPG use (0.17%/%).

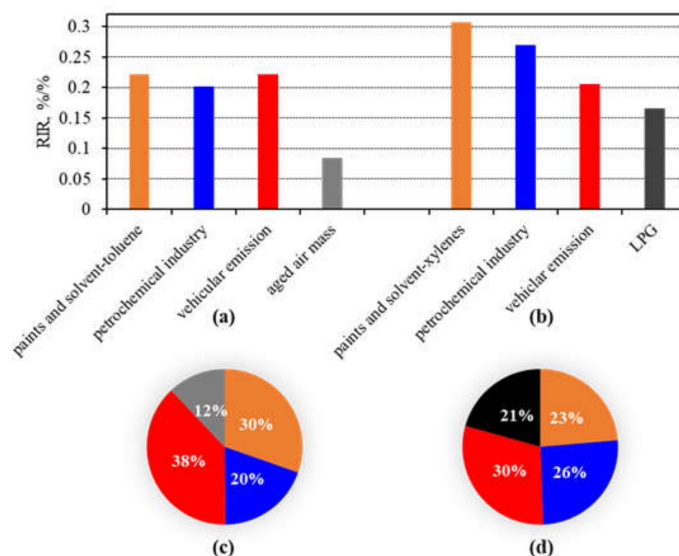


Figure 11. The *RIR* values for anthropogenic NMHCs from different PMF-resolved sources (a) at the DSH site and (b) the PD site, and relative contributions of different sources to O₃ formation (c) at the DSH site and (d) at the PD site during pollution episodes (11–16 July and 18–26 July).

Relative contributions of different sources to O₃ formation were calculated based on NMHC mixing ratios and *RIR* values (Equation (3)). As shown in Figure 11c, the two sources related to vehicular emission and paint and solvent use were the largest two contributors to O₃ formation at the DSH site, with values of 38% and 30%, followed by the petrochemical industry (20%) and aged air mass (12%). At the PD site, the contribution of vehicular emission to O₃ formation was 30%, higher than that for the petrochemical industry (20%), paint and solvent use-xylenes (23%), and LPG use (21%). It can be found that contributions of different sources to O₃ formation showed significant discrepancy with contributions of individual sources to NMHC mixing ratios (Figure 11c,d). From the perspective of O₃ formation, those sources characterized by a high abundance of reactive species, such as the petrochemical industry and paint and solvent use, showed higher contributions. This implied that those sources should be given priority to reduce their emissions to control O₃.

3.4. Case Study: Influence of Transport on O₃ Sensitivity

The DSH site is located at the junction of the Shanghai, Jiangsu, and Zhejiang provinces, and transport of air masses is a possible influence factor on O₃ formation. Two O₃ episode days with different O₃ formation regimes (11 and 15 July) were selected to compare NMHCs/NO_x, air mass paths, and NMHCs sources.

The OH reactivity of NMHCs (L_{OH}) was calculated using the NMHC mixing ratios by multiplying the reaction rate constant with OH radical (k_{OH}) for individual species [29,48]. The daytime average L_{OH} values of NMHCs on 11 and 15 July were 4.85 s^{-1} and 5.74 s^{-1} , respectively. The daytime average L_{OH}/NO_x increased from $0.16 \text{ s}^{-1}/\text{ppbV}$ on 11 July to $0.21 \text{ s}^{-1}/\text{ppbV}$ on 15 July. The noteworthy increase in $L_{OH}(\text{NMHCs})/\text{NO}_x$ is the possible reason for the change in O₃ formation regime from an NMHC-limited regime on 11 July to a transition regime on 15 July.

There are no data showing that the local emission intensity of NMHCs and NO_x at the DSH site changed in July 2017; thus, the change in $L_{OH}(\text{NMHCs})/\text{NO}_x$ was possibly related to air mass path changes. The backward trajectory of the air masses from 7:00 a.m.–7:00 p.m. on 11 and 15 July was analyzed using the Meteoinfo model developed by Wang [49]. As shown in Figure 12, the air masses on July 11 were mainly from the south and southwest (red lines in Figure 12), passing through several small industrial zones (A–C), where wooden furniture, machinery equipment, and pesticide manufacturing are the main industries. The air masses on July 15 were mainly from the south (blue

lines in Figure 12), passing through one of the largest petrochemical industry zones in the OBM region (D in Figure 12). The main industries in this region are oil refining and ethylene industries and their downstream industries, such as synthetic rubber, synthetic resin, synthetic fibers, and relevant raw materials [50]. Previous studies showed that the NMHC emission intensity in the southwest area of the DSH site is relatively low, while, in the south, the Hangzhou bay region presents a concentrated high NMHC emission intensity [50,51]. Therefore, air masses on 15 July possibly carried more NMHCs than those on 11 July. To check these results from back trajectory analysis, the NMHC source structures on these two days were compared. Relative contributions of paint and solvent use-toluene and the petrochemical industry on 11 July were 30% and 16%, respectively. However, the petrochemical industry was the largest contributor to NMHCs on July 15, with a value of 28%. Meanwhile, the relative contribution of paint and solvent use-toluene decreased to 19%. The changes in NMHC sources during these two episodes were consistent with the results from the air mass transport analysis. It should be noted that, since back trajectory analysis is only a qualitative method to discuss the influence of transport, a more quantitative evaluation on transport can be conducted using an air quality model in further research.

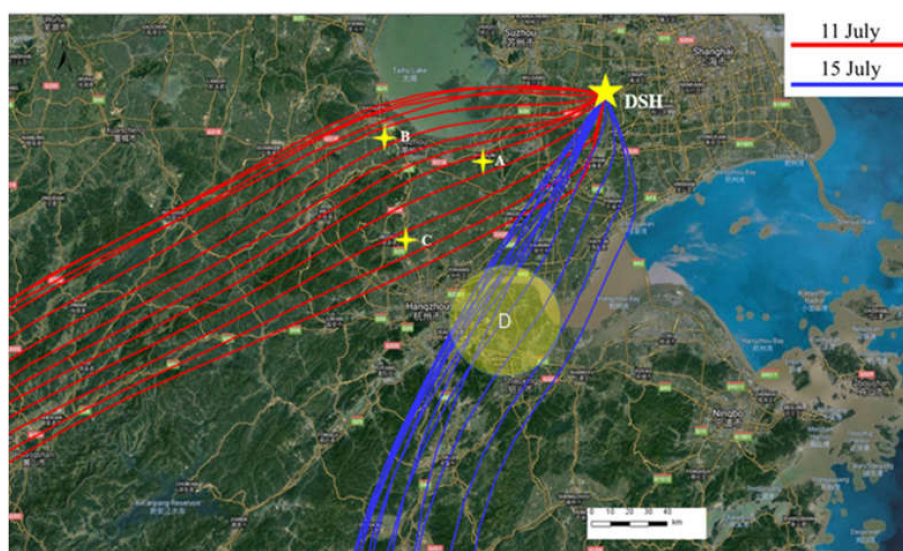


Figure 12. Backward trajectories at the DSH site from 7:00 a.m.–7:00 p.m.1 on 11 July (red lines) and 15 July (blue lines) 2017.

4. Conclusions

To better understand the sensitivity of O_3 formation to its precursors and contributions of different sources in O_3 formation in the YRD region, online measurements of O_3 , NO_x , NMHCs, and CO were conducted at an urban site (PD) and a suburban site (DSH) in Shanghai from 1–31 July 2017. The DMA-1h O_3 concentrations were in the ranges of 30.3 ppbV–167.5 ppbV and 35.9 ppbV–169.4 ppbV at the PD and the DSH sites, respectively. O_3 concentrations showed an average diurnal variation pattern with a peak at 12:00–1:00 p.m., while NMHCs and NO_x showed higher concentrations at night and in the morning.

The O_3 sensitivity to its precursors on 15 O_3 pollution episode days (i.e., O_3 concentration exceeding national air quality standard) were analyzed using the OBM. The average *RIR* values for AHC and NHC during O_3 pollution episodes at these sites were 0.26–0.44%/ and 0.30–0.36%/ , suggesting that reducing AHC and NHC would result in O_3 decrease. The average *RIR* value for NO_x at the DSH site was 0.07%/ ; however, that for the PD site was −0.11%/ . This means that reducing NO_x at the DSH site would be beneficial for O_3 control (i.e., transition regime), but reducing NO_x at the PD site could possibly lead to O_3 increase (i.e., NMHC-limited regime). The O_3 formation regime at the urban site agreed with results from previous studies, while the O_3 sensitivity at the suburban

site determined by the OBM in this study was different from previous studies. Based on *RIR* values, xylenes, propene, trans/cis-butene, propane, ethene, and 1,2,3-trimethylbenzene were found to be key anthropogenic NMHC species in O₃ formation.

Four anthropogenic sources for NMHCs were identified by the PMF model at both sites. At the DSH site, aged air mass was found to be the largest contributor to NMHCs mixing ratios from 1–31 July, with an average value of 32%, followed by vehicular emission (30%), paint and solvent use-toluene (24%), and the petrochemical industry (14%). At the PD site, LPG use and vehicular emission were the largest two contributors to NMHC mixing ratios, with respective values of 33% and 30%, followed by the petrochemical industry (21%) and paint and solvent use-xylenes (16%).

To estimate the relative contributions of different sources in O₃ formation, the PMF-resolved NMHC concentrations for different sources were then input into the OBM to calculate *RIR* values for each source during O₃ pollution episodes. Among the four sources at the DSH site, the *RIR* values for paint and solvent use-toluene and vehicular emission were close, with a value of 0.22%/%, higher than that for the petrochemical industry (0.20%/%) and that for aged air mass (0.08%/%). At the PD site, the largest *RIR* value was from paint and solvent use-xylenes (0.31%/%), followed by the petrochemical industry (0.27%/%), vehicular emission (0.21%/%), and LPG use (0.17%/%). The two sources related to vehicular emission and paint and solvent use were the largest two contributors to O₃ formation at the DSH site, with values of 38% and 30%, followed by the petrochemical industry (20%) and aged air mass (12%). At the PD site, the contribution of vehicular emission to O₃ formation was 30%, higher than those for petrochemical industry (20%), paint and solvent use-xylene (23%), and LPG use (21%). The significant difference in source contributions in O₃ formation and NMHC mixing ratios implies that NMHC levels and reactivity should both be considered in the development of O₃ control measures.

The influence of transport on O₃ sensitivity was preliminarily identified by comparing O₃ sensitivity at the DHS site between 11 and 15 July. The air masses on 11 July were mainly from the south and southwest, passing through several small industrial zones, while air masses on 15 July were from the south, passing one of largest petrochemical zones in YRD. Consequently, the NMHC/NO_x on 15 July was significantly higher than that for 11 July; thus, the O₃–NMHC–NO_x sensitivity changed from an NMHC-limited regime on 11 July to a transition regime on 15 July. This finding reveals that O₃ formation in Shanghai is not only related to local emissions but also influenced by emissions from neighboring provinces.

The findings on O₃–NMHC–NO_x sensitivity, contributions of different sources in O₃ formation, and influence of transport in this study would be useful for policymakers to develop O₃ and NMHC control strategies in the YRD and other regions of China. Nevertheless, it should be noted that these results were based on limited measurements for one month and two sites; therefore, their spatial and temporal representativeness should be considered when applying them. In addition, more quantitative analyses on transport and a further evaluation on the uncertainty of OBM are still needed to increase the reliability of these methods.

Supplementary Materials: The following are available online at <http://www.mdpi.com/2073-4433/11/3/295/s1>, Table S1. Reactions related to OH radical in the OBM, Table S2. Reactions related to HO₂ radical in the OBM.

Author Contributions: All authors have read and agree to the published version of the manuscript. Conceptualization, M.W. and Y.D.; methodology, M.W., W.J., H.C., D.J., and Y.L.; software, W.J.; investigation, Y.D.; resources, Y.D. and Q.F.; data curation, H.L., H.C., D.J., and Y.L.; writing—original draft preparation, H.L.; writing—review and editing, M.W. and K.H.; supervision, Q.F.; funding acquisition, Y.D., Q.F. and M.W.

Funding: This research was funded by the Scientific Research Project of Shanghai Science and Technology Commission (grant number 16DZ1204606), the National Key R&D Program of China (grant number 2016YFC0202200), and the National Natural Science Foundation of China (grant number 41505113).

Acknowledgments: We are grateful for financial support from the Scientific Research Project of Shanghai Science and Technology Commission (grant number 16DZ1204606), the National Key R&D Program of China (grant number 2016YFC0202200), and the National Natural Science Foundation of China (grant number 41505113). And we would like to show deep thankfulness to reviewers and editors who have contributed valuable comments to improve the quality of the paper.

Conflicts of Interest: The authors declare no conflict of interest.

References

1. The China Environment Report 2017. Available online: <http://datacenter.mee.gov.cn> (accessed on 31 May 2018).
2. Li, K.; Jacob, D.J.; Liao, H.; Shen, L.; Zhang, Q.; Bates, K.H. Anthropogenic drivers of 2013–2017 trends in summer surface ozone in China. *Proc. Natl. Acad. Sci. USA* **2018**, *116*, 422–427. [[CrossRef](#)] [[PubMed](#)]
3. Wang, T.; Xue, L.; Brimblecombe, P.; Lam, Y.F.; Li, L.; Zhang, L. Ozone pollution in China: A review of concentrations, meteorological influences, chemical precursors, and effects. *Sci. Total Environ.* **2017**, *575*, 1582–1596. [[CrossRef](#)] [[PubMed](#)]
4. Sillman, S. Some theoretical results concerning O₃-NO_x-VOC chemistry and NO_x-VOC indicators. *J. Geophys. Res. Atmos.* **2002**, *107*, ACH-26. [[CrossRef](#)]
5. Ibarra-Berastegi, G.; Elías, A.; Agirre, E.; Uria, J. Short-term, real-time forecasting of hourly ozone, NO₂ and NO levels by means of multiple linear regression modelling. *Environ. Sci. Pollut. Res.* **2001**, *8*, 250. [[CrossRef](#)]
6. Li, L.; Chen, C.H.; Huang, C.; Huang, H.Y.; Zhang, G.F.; Wang, Y.J.; Wang, H.L.; Lou, S.R.; Qiao, L.P.; Zhou, M.; et al. Process analysis of regional ozone formation over the Yangtze River Delta, China using the Community Multi-scale Air Quality modeling system. *Atmos. Chem. Phys.* **2012**, *12*, 10971–10987. [[CrossRef](#)]
7. He, Z.; Wang, X.; Ling, Z.; Zhao, J.; Guo, H.; Shao, M.; Wang, Z. Contributions of different anthropogenic volatile organic compound sources to ozone formation at a receptor site in the Pearl River Delta region and its policy implications. *Atmos. Chem. Phys.* **2019**, *19*, 8801–8816. [[CrossRef](#)]
8. Wang, M.; Shao, M.; Chen, W.; Yuan, B.; Lu, S.; Zhang, Q.; Zeng, L.; Wang, Q. A temporally and spatially resolved validation of emission inventories by measurements of ambient volatile organic compounds in Beijing, China. *Atmos. Chem. Phys.* **2014**, *14*, 5871–5891. [[CrossRef](#)]
9. Liu, Z.; Wang, Y.; Vrekoussis, M.; Richter, A.; Wittrock, F.; Burrows, J.P.; Shao, M.; Chang, C.C.; Liu, S.C.; Wang, H.L.; et al. Exploring the missing source of glyoxal (CHOCHO) over China. *Geophys. Res. Lett.* **2012**, *39*. [[CrossRef](#)]
10. Xu, Z.; Huang, X.; Nie, W.; Chi, X.; Xu, Z.; Zheng, L.; Sun, P.; Ding, A. Influence of synoptic condition and holiday effects on VOCs and ozone production in the Yangtze River Delta region, China. *Atmos. Environ.* **2017**, *168*, 112–124. [[CrossRef](#)]
11. Tan, Z.; Lu, K.; Dong, H.; Hu, M.; Li, X.; Liu, Y.; Lu, S.; Shao, M.; Su, R.; Wang, H.; et al. Explicit diagnosis of the local ozone production rate and the ozone-NO_x-VOC sensitivities. *Sci. Bull.* **2018**, *63*, 1067–1076. [[CrossRef](#)]
12. Liu, Y.; Shao, M.; Fu, L.; Lu, S.; Zeng, L.; Tang, D. Source profiles of volatile organic compounds (VOCs) measured in China: Part I. *Atmos. Environ.* **2008**, *42*, 6247–6260. [[CrossRef](#)]
13. Tang, W.; Zhao, C.; Geng, F.; Peng, L.; Zhou, G.; Gao, W.; Xu, J.; Tie, X. Study of ozone “weekend effect” in Shanghai. *Sci. China Ser. D Earth Sci.* **2008**, *51*, 1354–1360. [[CrossRef](#)]
14. Ran, L.; Zhao, C.; Geng, F.; Tie, X.; Tang, X.; Peng, L.; Zhou, G.; Yu, Q.; Xu, J.; Guenther, A. Ozone photochemical production in urban Shanghai, China: Analysis based on ground level observations. *J. Geophys. Res. Atmos.* **2009**, *114*. [[CrossRef](#)]
15. Tan, Z.; Lu, K.; Jiang, M.; Su, R.; Wang, H.; Lou, S.; Fu, Q.; Zhai, C.; Tan, Q.; Yue, D.; et al. Daytime atmospheric oxidation capacity in four Chinese megacities during the photochemically polluted season: A case study based on box model simulation. *Atmos. Chem. Phys.* **2019**, *19*, 3493–3513. [[CrossRef](#)]
16. Wang, H.L.; Chen, C.H.; Wang, Q.; Huang, C.; Su, L.Y.; Huang, H.Y.; Lou, S.R.; Zhou, M.; Li, L.; Qiao, L.P.; et al. Chemical loss of volatile organic compounds and its impact on the source analysis through a two-year continuous measurement. *Atmos. Environ.* **2013**, *80*, 488–498. [[CrossRef](#)]
17. Cai, C.J.; Geng, F.H.; Tie, X.X.; Yu, Q.O.; An, J.L. Characteristics and source apportionment of VOCs measured in Shanghai, China. *Atmos. Environ.* **2010**, *44*, 5005–5014. [[CrossRef](#)]
18. Song, M.; Liu, X.; Tan, Q.; Feng, M.; Qu, Y.; An, J.; Zhang, Y.J.E.P. Characteristics and formation mechanism of persistent extreme haze pollution events in Chengdu, southwestern China. *Environ. Pollut.* **2019**, *251*, 1–12. [[CrossRef](#)] [[PubMed](#)]
19. Paatero, P.; Tapper, U. Positive matrix factorization: A non-negative factor model with optimal utilization of error estimates of data values. *Environmetrics* **1994**, *5*, 111–126. [[CrossRef](#)]

20. Paatero, P. Least Squares Formulation of Robust Non-Negative Factor Analysis. *Chemom. Intell. Lab. Syst. Chemom. Intell. Lab. Syst.* **1997**, *37*, 23–35. [[CrossRef](#)]
21. Cardelino, C.A.; Chameides, W.L. An Observation-Based Model for Analyzing Ozone Precursor Relationships in the Urban Atmosphere. *J. Air Waste Manag. Assoc.* **1995**, *45*, 161–180. [[CrossRef](#)]
22. Chan, C.Y.; Chan, L.Y. Effect of meteorology and air pollutant transport on ozone episodes at a subtropical coastal Asian city, Hong Kong. *J. Geophys. Res. Atmos.* **2000**, *105*, 20707–20724. [[CrossRef](#)]
23. Nair, P.R.; Chand, D.; Lal, S. Temporal variations in surface ozone at Thumba (8.6 N, 77 E)—a tropical coastal site in India. *Atmos. Environ.* **2002**, *36*, 603–610. [[CrossRef](#)]
24. Lu, K.D.; Rohrer, F.; Holland, F.; Fuchs, H.; Bohn, B.; Brauers, T.; Chang, C.C.; Häseler, R.; Hu, M.; Kita, K.; et al. Observation and modelling of OH and HO₂ concentrations in the Pearl River Delta 2006: A missing OH source in a VOC rich atmosphere. *Atmos. Chem. Phys.* **2012**, *12*, 1541–1569. [[CrossRef](#)]
25. Lu, K.D.; Hofzumahaus, A.; Holland, F.; Bohn, B.; Brauers, T.; Fuchs, H.; Hu, M.; Häseler, R.; Kita, K.; Kondo, Y. Missing OH source in a suburban environment near Beijing: Observed and modelled OH and HO₂ concentrations in summer 2006. *Atmos. Chem. Phys.* **2013**, *13*, 1057–1080. [[CrossRef](#)]
26. Wang, Y.; Guo, H.; Zou, S.; Lyu, X.; Ling, Z.; Cheng, H.; Zeren, Y. Surface O₃ photochemistry over the South China Sea: Application of a near-explicit chemical mechanism box model. *Environ. Pollut.* **2018**, *234*, 155–166. [[CrossRef](#)] [[PubMed](#)]
27. Tan, Z.; Fuchs, H.; Lu, K.; Hofzumahaus, A.; Bohn, B.; Broch, S.; Dong, H.; Gomm, S.; Häseler, R.; He, L.; et al. Radical chemistry at a rural site (Wangdu) in the North China Plain: Observation and model calculations of OH, HO₂ and RO₂ radicals. *Atmos. Chem. Phys.* **2017**, *17*, 663–690. [[CrossRef](#)]
28. Nan, J.; Wang, S.; Guo, Y.; Xiang, Y.; Zhou, B. Study on the daytime OH radical and implication for its relationship with fine particles over megacity of Shanghai, China. *Atmos. Environ.* **2017**, *154*, 167–178. [[CrossRef](#)]
29. Atkinson, R.; Baulch, D.L.; Cox, R.A.; Crowley, J.N.; Hampson, R.F.; Hynes, R.G.; Jenkin, M.E.; Rossi, M.J.; Troe, J.; Wallington, T.J. Evaluated kinetic and photochemical data for atmospheric chemistry: Volume IV—gas phase reactions of organic halogen species. *Atmos. Chem. Phys.* **2008**, *8*, 4141–4496. [[CrossRef](#)]
30. Parrish, D.D.; Stohl, A.; Forster, C.; Atlas, E.L.; Blake, D.R.; Goldan, P.D.; Kuster, W.C.; de Gouw, J.A. Effects of mixing on evolution of hydrocarbon ratios in the troposphere. *J. Geophys. Res. Atmos.* **2007**, *112*. [[CrossRef](#)]
31. Tie, X.; Geng, F.; Guenther, A.; Cao, J.; Greenberg, J.; Zhang, R.; Apel, E.; Li, G.; Weinheimer, A.; Chen, J.; et al. Megacity impacts on regional ozone formation: Observations and WRF-Chem modeling for the MIRAGE-Shanghai field campaign. *Atmos. Chem. Phys.* **2013**, *13*, 5655–5669. [[CrossRef](#)]
32. Geng, F.; Tie, X.; Xu, J.; Zhou, G.; Peng, L.; Gao, W.; Tang, X.; Zhao, C. Characterizations of ozone, NO_x, and VOCs measured in Shanghai, China. *Atmos. Environ.* **2008**, *42*, 6873–6883. [[CrossRef](#)]
33. Ran, L.; Zhao, C.S.; Xu, W.Y.; Han, M.; Lu, X.Q.; Han, S.Q.; Lin, W.L.; Xu, X.B.; Gao, W.; Yu, Q. Ozone production in summer in the megacities of Tianjin and Shanghai, China: A comparative study. *Atmos. Chem. Phys.* **2012**, *12*, 7531–7542. [[CrossRef](#)]
34. Li, L.; Chen, C.; Huang, C.; Huang, H.; Zhang, G.; Wang, Y.; Chen, M.; Wang, H.; Chen, Y.; Streets, D.G.; et al. Ozone sensitivity analysis with the MM5-CMAQ modeling system for Shanghai. *J. Environ. Sci.* **2011**, *23*, 1150–1157. [[CrossRef](#)]
35. Tie, X.; Geng, F.; Peng, L.; Gao, W.; Zhao, C. Measurement and modeling of O₃ variability in Shanghai, China: Application of the WRF-Chem model. *Atmos. Environ.* **2009**, *43*, 4289–4302. [[CrossRef](#)]
36. Xue, L.; Wang, T.; Gao, J.; Ding, A.; Zhou, X.; Blake, D.; Wang, X.; Saunders, S.; Fan, S.; Zuo, H.; et al. Ground-level ozone in four Chinese cities: Precursors, regional transport and heterogeneous processes. *Atmos. Chem. Phys.* **2014**, *14*, 13175–13188. [[CrossRef](#)]
37. Zheng, C.; Shen, J.; Zhang, Y.; Huang, W.; Zhu, X.; Wu, X.; Chen, L.; Xiang, G.; Cen, K. Quantitative assessment of industrial VOC emissions in China: Historical trend, spatial distribution, uncertainties, and projection. *Atmos. Environ.* **2017**, *150*, 116–125. [[CrossRef](#)]
38. Gao, W.; Tie, X.; Xu, J.; Huang, R.; Mao, X.; Zhou, G.; Chang, L. Long-term trend of O₃ in a mega City (Shanghai), China: Characteristics, causes, and interactions with precursors. *Sci. Total Environ.* **2017**, *603*, 425–433. [[CrossRef](#)]
39. Bernard, A.; Frédéric, C.; Sophie, L. Contribution of HONO sources to the NO_x/HO_x/O₃ chemistry in the polluted boundary layer. *Atmos. Environ.* **2003**, *37*, 487–498.

40. Elshorbany, Y.F.; Steil, B.; Brühl, C.; Lelieveld, J. Impact of HONO on global atmospheric chemistry calculated with an empirical parameterization in the EMAC model. *Atmos. Chem. Phys.* **2012**, *12*, 9977–10000. [[CrossRef](#)]
41. Yuan, B.; Shao, M.; Lu, S.H.; Wang, B. Source profiles of volatile organic compounds associated with solvent use in Beijing, China. *Atmos. Environ.* **2010**, *44*, 1919–1926. [[CrossRef](#)]
42. Zheng, J.; Yu, Y.; Mo, Z.; Zhang, Z.; Wang, X.; Yin, S.; Peng, K.; Yang, Y.; Feng, X.; Cai, H. Industrial sector-based volatile organic compound (VOC) source profiles measured in manufacturing facilities in the Pearl River Delta, China. *Sci. Total Environ.* **2013**, *456*, 127–136. [[CrossRef](#)] [[PubMed](#)]
43. Mo, Z.; Shao, M.; Lu, S.; Qu, H.; Zhou, M.; Sun, J.; Gou, B. Process-specific emission characteristics of volatile organic compounds (VOCs) from petrochemical facilities in the Yangtze River Delta, China. *Sci. Total Environ.* **2015**, *533*, 422–431. [[CrossRef](#)] [[PubMed](#)]
44. Mo, Z.W.; Shao, M.; Lu, S.H. Compilation of a source profile database for hydrocarbon and OVOC emissions in China. *Atmos. Environ.* **2016**, *143*, 209–217. [[CrossRef](#)]
45. Hao, H.; Liu, Z.; Zhao, F.; Li, W. Natural gas as vehicle fuel in China: A review. *Renew. Sustain. Energy Rev.* **2016**, *62*, 521–533. [[CrossRef](#)]
46. Katzenstein, A.S.; Doezema, L.A.; Simpson, I.J.; Blake, D.R.; Rowland, F.S. Extensive regional atmospheric hydrocarbon pollution in the southwestern United States. *Proc. Natl. Acad. Sci. USA* **2003**, *100*, 11975–11979. [[CrossRef](#)] [[PubMed](#)]
47. Blake, D.R.; Rowland, F.S. Urban leakage of liquefied petroleum gas and its impact on Mexico City air quality. *Science* **1995**, *269*, 953–956. [[CrossRef](#)]
48. Praplan, A.P.; Pfannerstill, E.Y.; Williams, J.; Hellén, H. OH reactivity of the urban air in Helsinki, Finland, during winter. *Atmos. Environ.* **2017**, *169*, 150–161. [[CrossRef](#)]
49. Wang, Y.Q. An Open Source Software Suite for Multi-Dimensional Meteorological Data Computation and Visualisation. *J. Open Res. Softw.* **2019**, *7*, 21. [[CrossRef](#)]
50. Huang, C.; Chen, C.H.; Li, L.; Cheng, Z.; Wang, H.L.; Huang, H.Y.; Chen, Y.R. Emission inventory of anthropogenic air pollutants and VOC species in the Yangtze River Delta region, China. *Atmos. Chem. Phys.* **2011**, *11*, 4105–4120. [[CrossRef](#)]
51. Fu, X.; Wang, S.; Zhao, B.; Xing, J.; Cheng, Z.; Liu, H.; Hao, J. Emission inventory of primary pollutants and chemical speciation in 2010 for the Yangtze River Delta region, China. *Atmos. Environ.* **2013**, *70*, 39–50. [[CrossRef](#)]



© 2020 by the authors. Licensee MDPI, Basel, Switzerland. This article is an open access article distributed under the terms and conditions of the Creative Commons Attribution (CC BY) license (<http://creativecommons.org/licenses/by/4.0/>).